

Arterial input function estimation compensating for inflow and partial voluming in dynamic contrast-enhanced MRI

Tseng, C.; Nagtegaal, M.A.; van Osch, Matthias J P; Jaspers, Jaap; Méndez Romero, Alejandra; Wielopolski, Piotr; Smits, M.; Vos, F.M.

DOI

[10.1002/nbm.5225](https://doi.org/10.1002/nbm.5225)

Publication date

2024

Document Version

Final published version

Published in

NMR in Biomedicine

Citation (APA)

Tseng, C., Nagtegaal, M. A., van Osch, M. J. P., Jaspers, J., Méndez Romero, A., Wielopolski, P., Smits, M., & Vos, F. M. (2024). Arterial input function estimation compensating for inflow and partial voluming in dynamic contrast-enhanced MRI. *NMR in Biomedicine*, 37(12), Article e5225. <https://doi.org/10.1002/nbm.5225>

Important note

To cite this publication, please use the final published version (if applicable). Please check the document version above.



Copyright

Other than for strictly personal use, it is not permitted to download, forward or distribute the text or part of it, without the consent of the author(s) and/or copyright holder(s), unless the work is under an open content license such as Creative Commons.

Takedown policy

Please contact us and provide details if you believe this document breaches copyrights. We will remove access to the work immediately and investigate your claim.

Arterial input function estimation compensating for inflow and partial voluming in dynamic contrast-enhanced MRI

Chih-Hsien Tseng^{1,2,3}  | Martijn A. Nagtegaal^{1,4} | Matthias J.P. van Osch^{2,3,4}  |
Jaap Jaspers^{3,5} | Alejandra Mendez Romero^{3,5} | Piotr Wielopolski⁶ |
Marion Smits^{2,6,7} | Frans M. Vos^{1,2,3,6}

¹Department of Imaging Physics, Delft University of Technology, Delft, the Netherlands

²Medical Delta, Delft, the Netherlands

³HollandPTC Consortium—Erasmus MC, Rotterdam, Holland Proton Therapy Center, Delft, Leiden University Medical Center, Leiden and Delft University of Technology, Delft, the Netherlands

⁴C.J. Gorter MRI Center, Department of Radiology, Leiden University Medical Center, Leiden, the Netherlands

⁵Department of Radiotherapy, Erasmus MC Cancer Institute, University Medical Center Rotterdam, Rotterdam, The Netherlands

⁶Department of Radiology and Nuclear Medicine, Erasmus MC, University Medical Center Rotterdam, Rotterdam, the Netherlands

⁷Brain Tumour Center, Erasmus MC Cancer Institute, University Medical Center Rotterdam, Rotterdam, the Netherlands

Correspondence

Chih-Hsien Tseng, Department of Imaging Physics, Delft University of Technology, Lorentzweg 1, 2628 CJ, Delft, the Netherlands.

Email: c.tseng@tudelft.nl

Funding information

Medical Delta Cancer Diagnostics 3.0; HollandPTC-Varian Consortium

Both inflow and the partial volume effect (PVE) are sources of error when measuring the arterial input function (AIF) in dynamic contrast-enhanced (DCE) MRI. This is relevant, as errors in the AIF can propagate into pharmacokinetic parameter estimations from the DCE data. A method was introduced for flow correction by estimating and compensating the number of the perceived pulse of spins during inflow. We hypothesized that the PVE has an impact on concentration–time curves similar to inflow. Therefore, we aimed to study the efficiency of this method to compensate for both effects simultaneously. We first simulated an AIF with different levels of inflow and PVE contamination. The peak, full width at half-maximum (FWHM), and area under curve (AUC) of the reconstructed AIFs were compared with the true (simulated) AIF. In clinical data, the PVE was included in AIFs artificially by averaging the signal in voxels surrounding a manually selected point in an artery. Subsequently, the artificial partial volume AIFs were corrected and compared with the AIF from the selected point. Additionally, corrected AIFs from the internal carotid artery (ICA), the middle cerebral artery (MCA), and the venous output function (VOF) estimated from the superior sagittal sinus (SSS) were compared. As such, we aimed to investigate the effectiveness of the correction method with different levels of inflow and PVE in clinical data. The simulation data demonstrated that the corrected AIFs had only marginal bias in peak value, FWHM, and AUC. Also, the algorithm yielded highly correlated reconstructed curves over increasingly larger neighbourhoods surrounding selected arterial points in clinical data. Furthermore, AIFs measured from the ICA and MCA produced similar peak height and FWHM, whereas a significantly larger peak and lower FWHM was found compared with the VOF. Our findings indicate that the proposed method has high potential to compensate for PVE and inflow simultaneously. The corrected AIFs could thereby provide a stable input source for DCE analysis.

Abbreviations: AIF, arterial input function; AUC, area under the curve; BBB, blood–brain barrier; DCE, dynamic contrast-enhanced; EES, extravascular extracellular space; ETM, extended Tofts model; FOV, field of view; FWHM, full width at half-maximum; GBCA, gadolinium-based contrast agent; ICA, internal carotid artery; IDH, isocitrate dehydrogenase; MCA, middle cerebral artery; NRMSE, normalized root-mean-square error; PFP, peak FWHM product; PVE, partial volume effect; RIGEL, Radiotherapy in Isocitrate dehydrogenase mutated Glioma: Evaluation of Late outcomes; ROI, region of interest; SNR, signal-to-noise ratio; SSS, superior sagittal sinus; VOF, venous output function.

This is an open access article under the terms of the [Creative Commons Attribution-NonCommercial-NoDerivs](https://creativecommons.org/licenses/by-nc-nd/4.0/) License, which permits use and distribution in any medium, provided the original work is properly cited, the use is non-commercial and no modifications or adaptations are made.

© 2024 The Author(s). NMR in Biomedicine published by John Wiley & Sons Ltd.

KEYWORDS

arterial input function, DCE MRI, inflow effect, partial volume effect

1 | INTRODUCTION

Dynamic contrast-enhanced (DCE) MRI is an imaging method often used for estimating vascular properties, especially in oncological applications.¹ Essentially, a gadolinium-based contrast agent (GBCA) is administered intravenously, while dynamic T_1 -weighted images are acquired for several minutes at a medium temporal resolution (of the order of a few seconds). In normal brain tissue, an intact blood–brain barrier (BBB) prevents leakage of GBCA into tissue. However, impairment of the BBB resulting from disease processes can lead to leakage of GBCA from vessels to the extravascular space. To identify such BBB damage and quantify its extent, parameters including the time to the peak,² maximum intensity,³ area under the curve (AUC),⁴ wash-in slope, wash-out rate, and signal enhancement ratio⁵ can be derived from the DCE signal–intensity curve.⁶ Alternatively, tracer kinetic models enable estimation of vascular properties (as summarized by Khalifa et al.⁷). The extended Tofts model (ETM) is the most frequently applied model in tumour assessment. It assumes that the GBCA is distributed in two compartments: the blood plasma and the extravascular extracellular space (EES), adopting a bidirectional exchange of the tracer across the BBB.⁸ By fitting this model to the measured signal intensity, vascular parameters are obtained, for example, the volume transfer constant (K^{trans}), reflux exchange rate from EES to plasma (K_{ep}), fraction volume of plasma (V_p), and fraction volume of EES (V_e). These quantitative parameters were shown to provide relevant clinical information about the vasculature.^{9,10}

The arterial input function (AIF) plays a crucial role in the estimation of the aforementioned pharmacokinetic model parameters, as it serves as the input to the model. The AIF describes the contrast agent concentration in an artery feeding the tissue of interest as a function of time. The use of a population-average AIF has been proposed to simplify the fitting procedure and enhance the reproducibility of the parameter estimations.¹¹ However, a population-average AIF ignores the natural variation in individual subjects, which can propagate erroneously to vascular parameter estimations.^{12,13}

Simultaneously, there are also known issues with measuring a subject-specific AIF. In general, it is preferred that the AIF is obtained near the tissue of interest to reduce travel time (delay) and dispersion, so that the shape and amplitude of AIFs is represented accurately.¹⁴ However, in the smaller arteries and even in the larger brain-feeding arteries, limited spatial resolution can result in mixing of signals: the partial volume effect (PVE).^{15,16} As a consequence, signals from the artery and surrounding tissue are combined, which generally results in underestimation of the GBCA concentration. To deal with this, previous studies have suggested either normalizing the AIF with the concentration measured in the superior sagittal sinus (SSS),^{16,17} that is, the venous output function (VOF), or using the VOF itself as an input to the pharmacokinetic model.^{18,19} Nonetheless, Hansen et al.¹⁶ pointed out that normalization methods are only valid when the contribution of the tissue signal is limited. Furthermore, Cramer et al.²⁰ found that using the VOF might lead to biased pharmacokinetic analysis, due to the increased dispersion of the concentration–time curve.

Inflow effects have shown to affect the AIF, especially when it is measured in a larger artery, away from the site of interest.²¹ In general, it is assumed that the recorded signal reflects the steady-state magnetization. In tissue this is often a valid assumption, but it may not hold in arteries. Here, “fresh” spins arrive continuously in the image volume, which have received insufficient excitations to reach a steady state. Effectively, this results in a hyperintense signal in the baseline images and underestimation of the T_1 signal enhancement induced by the GBCA. Several methods for reducing the impact of inflow effects were proposed. For instance, a flow phantom could be used to calibrate the effect.²² However, such calibration is often sequence-, subject-, and system-dependent. Measuring the AIF downstream could significantly improve the accuracy, but this may not be applicable to all in vivo imaging situations.²³ As an alternative, the AIF can be measured from phase accumulation induced by higher magnetic susceptibility of GBCA. This approach is insensitive to inflow effects that merely act on the magnitude of the signal.²⁴ At the same time, however, this signal can suffer from phase wrapping and flow-induced phase shift. Yet other correction methods were designed for particular applications, for example, liver DCE imaging,^{25,26} and therefore are not generally applicable.

Recently, a method was proposed for correcting inflow effects by first estimating the perceived pulse number and then correcting for the inflow effect.²⁷ However, PVEs were not considered. In the current article, we aim to assess the efficacy of this algorithm to compensate for *both* inflow *and* PVEs simultaneously. We hypothesize that a PVE can be interpreted as an underestimation of the perceived pulse number due to its similar impact on concentration–time curves. Simulation data were used to evaluate the correction method and clinical datasets were applied to verify the applicability in practice.

2 | THEORY

In this section we define the theory that was initially applied merely for modelling and correcting of inflow contamination, namely a low number of perceived pulses. The full derivation of the introduced equations can be found in the appendix of van Schie et al.²⁷

2.1 | Signal expression

In a spoiled gradient echo sequence, the signal can be expressed as an excitation of the longitudinal magnetization $M_z(n)$ followed by T_2^* decay:

$$S(n) = \sin \alpha \cdot M_z(n) \cdot e^{-T_E/T_2^*}, \quad (1)$$

in which α is the flip angle, T_E is the echo time, T_2^* is the tissue-specific T_2^* decay time, and n represents the number of RF pulses perceived by the spins, which directly reflects the degree of saturation. Clearly, the T_2^* decay term may be neglected while the applied echo time is sufficiently small ($T_E \ll T_2^*$).

The expression for $M_z(n)$ is

$$M_z(n) = M_0 \cdot \left[\left(1 - \frac{1 - E_1}{1 - \cos \alpha \cdot E_1} \right) \cdot (\cos(\alpha) \cdot E_1)^n + \frac{1 - E_1}{1 - \cos \alpha \cdot E_1} \right], \quad (2)$$

where

$$E_1 = e^{-T_R/T_1}, \quad (3)$$

with M_0 the net magnetization in equilibrium, T_R the repetition time, and T_1 the longitudinal relaxation time. Notice that when the spins have received enough excitation pulses, which is usually achieved in stationary tissue due to a sufficiently large number of start-up excitations, the longitudinal magnetization reaches a steady state, in which $M_z(n)$ can be simplified as

$$M_z(n) = M_0 \cdot \left(\frac{1 - E_1}{1 - \cos \alpha \cdot E_1} \right). \quad (4)$$

The magnetic unit will not alter with increasing perceived pulse number n at some point. Notice that this “sufficient” pulse number to saturate the magnetization is dependent on the applied repetition time and flip angle. The MRI signal in an artery, however, frequently does not reach the steady state, because spins enter the field of view with an inadequate number of excitation pulses, albeit still holding to Equation (2). As a consequence, a higher signal is obtained from these spins, which are in a transient state compared with what would have been measured had they been in a steady state. This leads to the phenomenon of inflow artefacts due to flow enhancement.

2.2 | GBCA-induced signal change

Under the influence of the GBCA, relaxation rates are modulated by the contrast concentration C in plasma:

$$\frac{1}{T_1} = \frac{1}{T_{10}} + (1 - Hct) \cdot r_1 \cdot C, \quad (5)$$

and

$$\frac{1}{T_2^*} = \frac{1}{T_{20}^*} + (1 - Hct) \cdot r_2^* \cdot C, \quad (6)$$

in which T_{10} and T_{20}^* represent the initial longitudinal and transverse relaxation times, respectively, Hct is the hematocrit level, and r_1 and r_2^* denote the longitudinal and transverse relaxivity of the GBCA. As a result of this, the magnetization and the measured signal become functions of both C and perceived pulse number (n): $M_z(C, n)$ and $S(C, n)$.

The signal ratio, denoted as D , characterizes the relative change between the post-contrast and pre-contrast signal intensities, which can be expressed as

$$D(C, n) = \frac{S(C, n)}{S(0, n)} = \frac{M_z(C, n)}{M_z(0, n)} \cdot e^{-T_E \cdot r_2^* \cdot C}. \quad (7)$$

This signal ratio expression contains only two unknown terms, which are the contrast concentration (C) and the perceived pulse number (n).

2.3 | AIF model

The AIF model from Orton et al.²⁸ was integrated in this approach to facilitate the correction for inflow. This AIF model is defined as a sum of two functions, one describing the first passage of the contrast agent and the other describing the wash-out phase of the GBCA during the tail of the AIF. The bolus peak $C_B(t)$ is defined by

$$C_B(t - t_0) = a_B \cdot \mu_B^2 \cdot (t - t_0) \cdot e^{-\mu_B \cdot (t - t_0)}, \quad (8)$$

in which a_B represents the area under the curve of the bolus peak (which is related to the total injected concentration, see below), μ_B the decay rate, and t_0 the bolus arrival time. The tail function is expressed as a convolution of the bolus peak and a body transfer function $G(t)$:

$$G(t) = a_G \cdot e^{-\mu_G t}, \quad (9)$$

where a_G determines the starting level of this function and μ_G governs the decay rate, reflecting kidney function. Thus, the complete AIF is modelled as follows:

$$C_{\text{Orton}}(t, \theta) = C_B(t - t_0) + C_B(t - t_0) * G(t), \quad (10)$$

in which θ contains all parameters for the AIF:

$$\theta = [a_B, \mu_B, a_G, \mu_G, t_0]. \quad (11)$$

2.4 | Correction method

This section summarizes the correction method. For further details we refer to the comprehensive description in van Schie et al.²⁷

Previously, it was observed that the area under the first bolus peak is related to the ratio of contrast agent dose and cardiac output.²² Furthermore, both dose and cardiac output are generally proportional to body weight.²⁹ Accordingly, the parameter representing the area under the first bolus peak of the AIF model (a_B) was assumed to be constant across subjects. This constant was set to $50.58 \text{ mM} \cdot \text{s}^{-1}$ for a standard dosage ($0.1 \text{ mmol} \cdot \text{kg}^{-1}$),^{27,28} and was scaled linearly with the dose per body mass. Consequently, any discrepancies between the model and a measured signal-ratio curve were attributed to inflow effects, which were subsequently accounted for by estimating the perceived pulse number n .

To correct the measured AIF signal curve, the following minimization problem was solved:

$$(\hat{\theta}, \hat{n}) = \arg \min_{\theta, n} \|D_{\text{meas}}(t) - D(C_{\text{Orton}}(t, \theta), n)\|_2, \quad (12)$$

in which $D_{\text{meas}}(t)$ is the measured signal-ratio curve and $D(C_{\text{Orton}}(t, \theta), n)$ is the fitted signal-ratio curve incorporating Orton's AIF model. While doing so, the free model parameters in θ (Equation 11) and the perceived pulse number n were estimated. The estimated parameters were constrained to be positive, and were determined using a nonlinear least-squares regression method.

Essentially, the estimation of n involved comparing the full measured time-series data with the AIF model, rather than considering each time point separately. However, in practice some information might not be represented in the model, such as the presence of a second peak. To address this, the concentration $C(t)$ at each time point was subsequently re-estimated using the estimated pulse number (\hat{n}), by solving C in

$$D(C(t), \hat{n}) = D_{\text{meas}}(t). \quad (13)$$

In effect, this yielded the final AIF concentration curve compensating for inflow effects, and in this study we will study whether this also compensates for PVE.

3 | MATERIALS AND METHODS

3.1 | Simulation

The AIF model in Section 2.3 was used to generate a standardized AIF concentration curve using population-averaged parameters: $a_B = 50.58 \text{ mM} \cdot \text{s}^{-1}$, $\mu_B = 0.3 \text{ s}^{-1}$, $a_G = 0.02 \text{ s}^{-1}$, $\mu_G = 0.003 \text{ s}^{-1}$, and $t_0 = 15 \text{ s}$.²⁸ The AIF curve first served to compute a magnetic resonance (MR) signal curve according to Equation (1) (via Equations 2 and 3) with T_1 and T_2^* modulated by the contrast concentration. In this computation the following constants were applied. Hct: 0.45, T_{10} in blood: 1.8 s,³⁰ T_{20}^* in blood: 0.02 s,³¹ r_1 : $4.5 \text{ (mM} \cdot \text{s)}^{-1}$ for gadobutrol,³² theoretical r_2^* : $5.9 \text{ (mM} \cdot \text{s)}^{-1}$.^{33,34} This was done for a variety of perceived pulse numbers n , yielding different MR signal curves $S(C, n)$, each of which was normalized according to Equation (7). Notice that T_2^* decay was included, even though a small echo time was applied for the in vivo experiments. Inflow simulations ignoring T_2^* decay were also explored to verify its influence.

For tissue, the steady-state signal ($S'(\infty)$) was modelled assuming certain constants T_1 and T_2^* of 1.2 s and 0.08 s, respectively, and setting n equal to infinity in Equation (1). Finally, a linear combination of the AIF signal and the tissue signal was applied to include PVE in the simulations:

$$S_P(f, n) = (1 - f) \cdot S(n) + f \cdot S'(\infty), \quad (14)$$

with PVE fraction f . Thus, our partial volume model mixes a constant background signal $S'(\infty)$ into the (foreground) AIF signal. In the Appendix it is shown that the AIF signal under the influence of inflow (i.e., varying n) can be rewritten and approximated to obtain a similar representation. As a consequence, flow has an impact on the time-concentration curve highly comparable with PVE.

White Gaussian noise was added to the resulting signal intensity curves to achieve a signal-to-noise ratio (SNR) equal to 40 dB, that is, the same as the SNR of the baseline signals measured in the internal carotid artery (ICA) in our clinical data. Finally, the simulated signal-intensity curves were transformed into signal-ratio curves $D_{\text{simu}}(t)$ by normalizing with the averaged baseline signal (before contrast agent arrival).

3.2 | Validation

First, simulations were run with only inflow effects incorporated: the PVE fraction (f) in Equation (14) was set to 0, and $n \in \{40, 60, 80, 100, 120, 140\}$. For each n , 10,000 simulations were performed with different noise realizations yielding signal-ratio curves $D_{\text{simu}}(t)$. The correction algorithm was applied to each simulated signal curve to estimate the perceived pulse number, which was then used to reconstruct the AIF concentration curve (Section 2.4). Finally, the reconstructed AIF was supersampled 20 times to 0.1-second temporal resolution using piecewise cubic interpolation,³⁵ from which the peak value, full width at half-maximum (FWHM), and AUC were computed; these values were compared with the ground-truth values calculated from the simulated AIF (through the same interpolation procedure).

Then, partial voluming was included by increasing the PVE fraction (f) from 10% up to 50% for different n (see above); again 10,000 noise realizations with SNR equal to 40 dB were obtained for each setting. Subsequently, the correction algorithm was applied. To show the interaction between the correction for inflow and PVE, we employed both the true simulated pulse number (without PVE correction) and the estimated perceived pulse number to reconstruct the AIFs. Furthermore, the peak value and FWHM of both the uncorrected and the corrected AIFs were compared with the ground-truth values.

3.3 | Clinical data acquisition

3.3.1 | Patient cohort

Data in this study were acquired as part of an associated clinical study in Netherlands: the Radiotherapy in Isocitrate dehydrogenase (IDH) mutated Glioma: Evaluation of Late outcomes (RIGEL) study (trial identifier: NCT04304300). The first 10 patients who had histologically confirmed, IDH mutated glioma (WHO grade 2 or 3) and for whom the relevant imaging data were available were included in this sub-study. Informed consent was obtained from all subjects. Post-operative radiation therapy and chemotherapy were given to every patient after surgical tumour resection. MRI was performed before and approximately 4 months after radiation therapy. From three patients, DCE images were obtained before and after radiation therapy; from two patients, scans were only made post-treatment; and from five patients, only pre-treatment data were included.

3.3.2 | Imaging and injection protocol

Imaging was performed on a 3T MRI system (Signa Premier, GE Healthcare, Waukesha, WI, USA) using a 48-channel head coil in the Erasmus MC (Rotterdam, Netherlands).

DCE images were acquired using a differential subsampling with Cartesian ordering sequence³⁶ with TR/TE : 2.7/0.9 ms, flip angle: 14° ; field of view (FOV): $220 \times 220 \times 144 \text{ mm}^3$; matrix size: 128×128 , 72 slices; in-plane resolution: $1.7 \text{ mm} \times 1.7 \text{ mm}$; reconstructed resolution: $0.9 \text{ mm} \times 0.9 \text{ mm}$; slice thickness: 2 mm, temporal resolution: 2 s, to obtain 183 image volumes in total. The entire DCE sequence took 6 minutes 6 seconds. Some other sequences were also applied for clinical purposes, but these are not relevant for this article.

In each patient, 7.5 ml of Gadobutrol (Gadovist[®], Bayer, Germany), corresponding to a standard dose for a 75-kg patient, were automatically injected by a power injector. The contrast agent injections were started 20 seconds after the start of the DCE imaging to allow acquisition of sufficient averages of the contrast-free baseline signal.

3.3.3 | Pre-processing

All image processing was done with in-house created scripts in Matlab (version R2021b; MathWorks, Inc., Natick, Massachusetts, United States). Head motion between the dynamic scans was checked visually by monitoring the three cross-sectional lines of the central coronal, sagittal, and axial slices across time. Slight misalignment of the boundaries was observed in three cases; this was corrected by performing 3D rigid registration of the entire series to the first volume. We did not apply registration in the case without observed movement, to avoid introducing interpolation errors.

3.4 | AIF measurement

3.4.1 | Region-of-interest selection

In all patients of this study, regions in an artery were selected in the hemisphere contralateral to the tumour, to avoid any possible effects of the tumour on the AIF measurement. These regions of interest (ROIs) were delineated manually on a DCE volume after bolus arrival in which the arteries could be easily identified. Specifically, ROIs were drawn in the ICA and segments of the middle cerebral artery (MCA). Sampling of the AIF signals was performed before registration to the T_1 map to avoid additional blurring.

3.4.2 | Artificially increased PVE

To test whether the inflow correction method can also correct for PVE, one voxel of interest was placed at the center of the ICA in a proximal imaging plane for each patient. Then, the signal-time curve of this voxel was averaged with those of surrounding voxels by applying an increasing kernel size, from 3-by-3 to 9-by-9 voxels applied within plane. This was done to mimic increasing PVE at a fixed inflow effect.

3.4.3 | Downstream sampling the AIF

The inflow effect is expected to diminish gradually from ICA to MCA, due to increased exposure to excitation pulses. However, simultaneously it can be expected that PVE becomes more severe, since the diameter of the arteries become smaller. To test the sensitivity of our correction algorithm to these mixed effects, we measured the AIF in the ICA (AIF_{ICA}), M1 (AIF_{M1}), and M2 (AIF_{M2}) segments of the MCA. Accordingly, groups of nine voxels were selected in the ICA and the M1 and M2 segments of the MCA in each patient, for measuring the AIF from upstream to downstream in the same arterial territory. Subsequently, the signal over the ROI was averaged for each dynamic to obtain a signal-time intensity curve reflecting the AIF.

3.4.4 | Concentration estimation

Signal-ratio curves $D_{meas}(t)$ were first derived by dividing the time-signal intensity curves from each region by the mean of the first 10 baseline signals. Then, the correction algorithm described in Section 2.4 was applied to the AIF signal-ratio curves, estimating the perceived pulse number. Finally, we used the estimated pulse number to reconstruct the AIFs.

3.4.5 | AIF alternative

Conforming to an often-applied practical approach, we also measured the VOF from the SSS (VOF_{SSS}). As with the AIFs, ROIs consisting of nine voxels inside the SSS were delineated manually in an axial slice, after which mean signal–time intensity curves were obtained. Subsequently, contrast concentration curves were calculated as described in Section 2.1, asserting that the spins were in the steady state and assuming $T_{10} = 1.8$ s for blood.

3.4.6 | Evaluation

For assessing the influence of artificially increasing PVE, the estimated pulse number from each kernel was compared with the estimated pulse number of the central voxel. Also, the root-mean-square error was calculated from the difference between the corrected AIF and the one from the central voxel (serving as the gold standard reference) and normalized further with the peak value of the central voxel to deliver the normalized root-mean-square error (NRMSE).

The AIF_{ICA} , AIF_{M1} , AIF_{M2} , and VOF_{SSS} were compared based on the peak values, FWHMs, and products of the peak value and FWHM (i.e., the peak FWHM product, PFP, which is related to the area under the first bolus peak). Differences were assessed statistically using the Wilcoxon test. P values smaller than 0.05 were considered as statistically significant.

4 | RESULTS

4.1 | Simulation

Figure 1 shows (A) Orton's AIF model employed as calculated from population-averaged parameters, (B) MR signal-ratio curves including only inflow effects, and (C) signal-ratio curves affected by both inflow effects and PVE. Notice that no noise was added, so that the graphs show only the effects of inflow and PVE.

4.2 | Validation

In the following experiments, Gaussian noise was added before deriving signal-ratio curves. Error percentages of the estimated pulse number, reconstructed peak value, FWHM, and AUC from simulated data that only included inflow effects are shown in Figure 2. A bias of a few per cent (less than 3%) was observed in all the plotted parameters. The variance increased when stronger inflow effects, that is, lower n , were simulated. Figure S1 collates the same estimations, while T_2^* effects were not included in the simulations. No bias has been detected in this simulation.

As PVEs were introduced, the estimated pulse numbers gradually decreased when the partial volume fraction increased (Figure 3a). Simultaneously, only a little influence on peak values and FWHMs was observed for the corrected AIFs, showing that the inflow correction method also compensated for most of the PVE (Figure 3b,c). This complementary correction becomes even more biased when applying the real (input) pulse number to correct the AIFs, that is, reflecting “perfect” correction for only the inflow effects (Figure 3d,e).

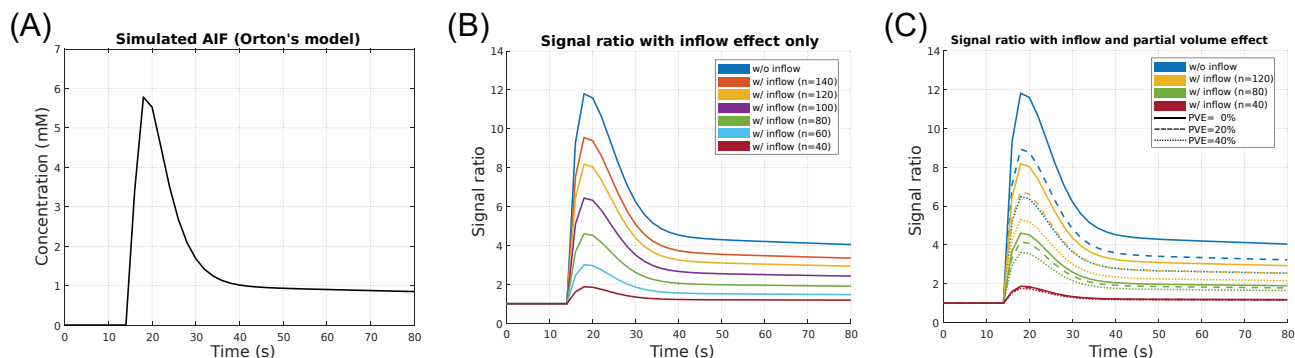


FIGURE 1 (A) Simulated AIF concentration curve from Orton's model, (B) signal-ratio curves from simulated AIF concentration curves with inflow effect only, and (C) likewise with partial voluming added. Notice that PVE led to similar underestimation of the AIF curves to inflow.

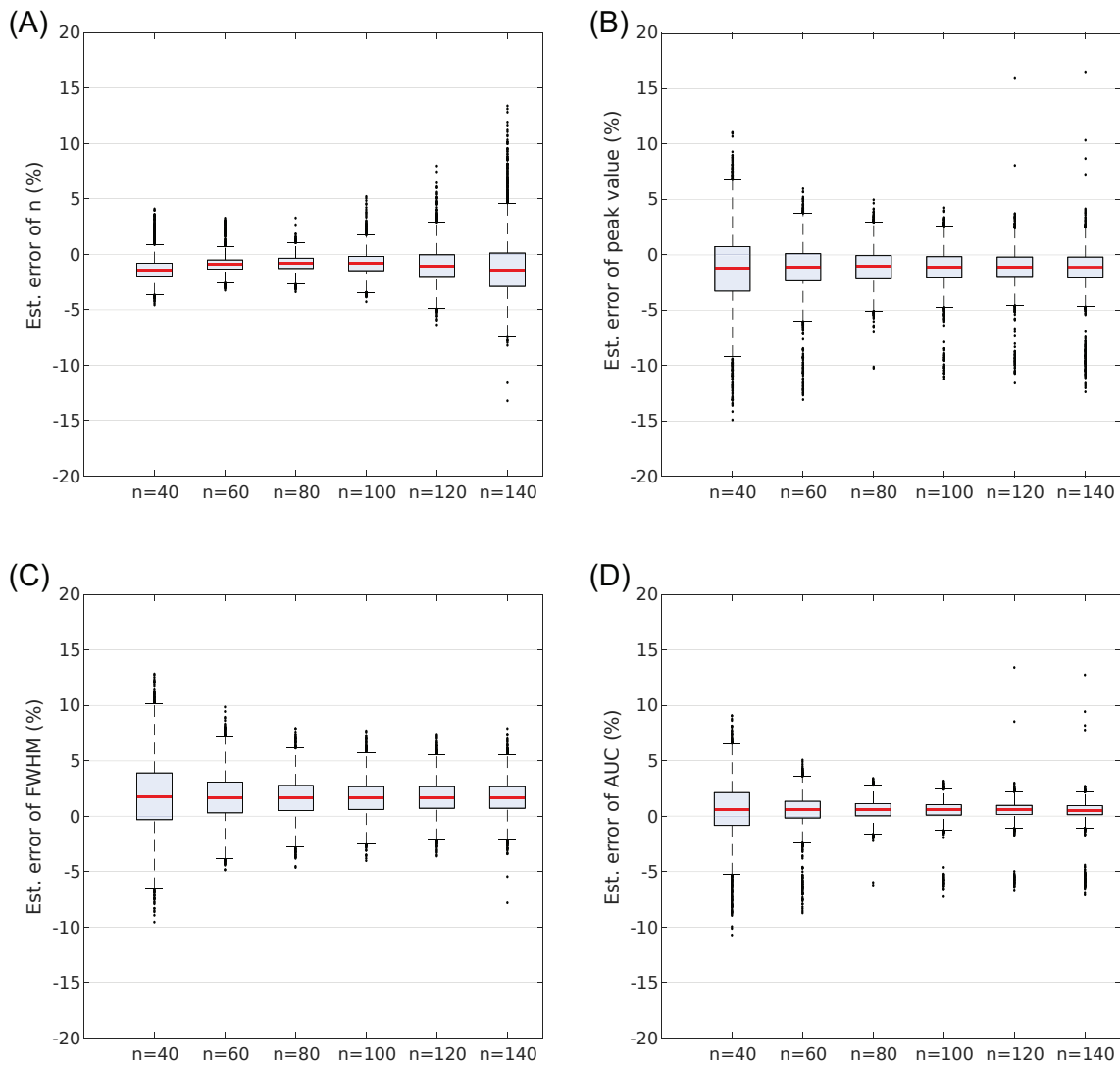


FIGURE 2 Error percentage of (A) estimated pulse number, (B) peak value, (C) FWHM, and (D) AUC of compensated AIFs while inflow and T_2^* effects are simulated.

4.3 | Correction in clinical data

4.3.1 | Artificially increased PVE

Figure 4 shows three representative examples of PVE compensation in different patients. Clearly, the AIFs were reconstructed faithfully even with large simulated partial voluming. A decrease in estimated pulse number with increasing PVE fraction was observed in every patient (Table 1). Furthermore, the NRMSE generally stayed small, albeit moderately higher with larger kernel sizes. Supplementary Figure S2 shows the detrimental effect on the signal curves and the reconstructions when a nearby vessel is included with a different enhancement time (i.e., arrival of the peak).

4.3.2 | AIF measurements upstream and downstream

A box plot of estimated pulse numbers for the AIFs and the VOF is included in supplementary Figure S3. Unsurprisingly, the VOF received markedly more excitation pulses than the AIFs did. Figure 5 shows the peak values, FWHMs, and PFPs of the three AIFs and the VOF for all subjects. The peak values in VOF_{SSS} were significantly lower than in AIF_{ICA} (p -value: 0.03) and AIF_{M1} (p -value: 0.04). The peak values in VOF_{SSS} and AIF_{M2} were not significantly different (p -value: 0.05). Significantly larger FWHMs were observed in VOF_{SSS} compared with AIF_{ICA} (p -value: 0.02) and

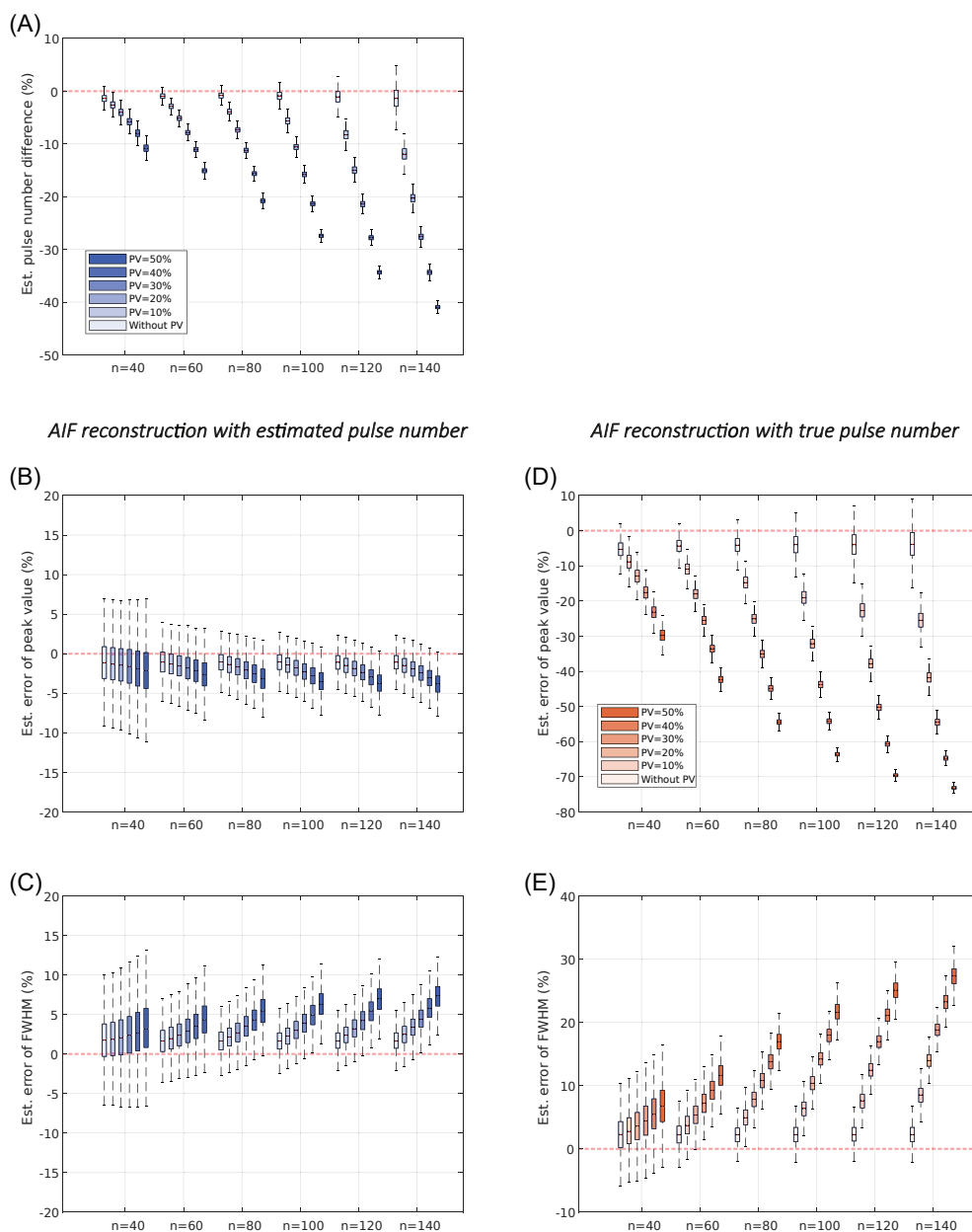


FIGURE 3 (A) Variation in the estimated pulse number when partial volume correction is included in simulated signal-ratio curves; (B) the peak value and (C) FWHM of the reconstructed AIF using the estimated pulse number; (D) error in peak value, and (e) FWHMs when using the true pulse number, that is, without partial volume correction during AIF reconstruction.

AIF_{M1} (p -value: 0.03). There was no significant difference between the FWHMs from VOF_{SSS} and AIF_{M1} (p -value: 0.10). Other comparisons, for example, the PFPs, yielded no significant differences.

5 | DISCUSSION

In this article, we studied the potential of a method to correct the AIF measured in DCE MRI simultaneously for PVE and inflow effects. This was inspired by the observation that PVE induces similar shape and amplitude changes of the AIF to inflow. In the Appendix, we underpin mathematically that the two effects indeed have a similar effect on AIF measurement, which also implies that they cannot be separated. Our results show that the correction algorithm sustains combined correction for both inflow effect and PVE.

While inflow correction has been widely studied, PVE on AIF measurement remains a challenging issue. Practically, the temporal resolution is often maximized for obtaining high-quality AIFs and high accuracy and precision of permeability estimates.³⁷ While doing so, the imaging

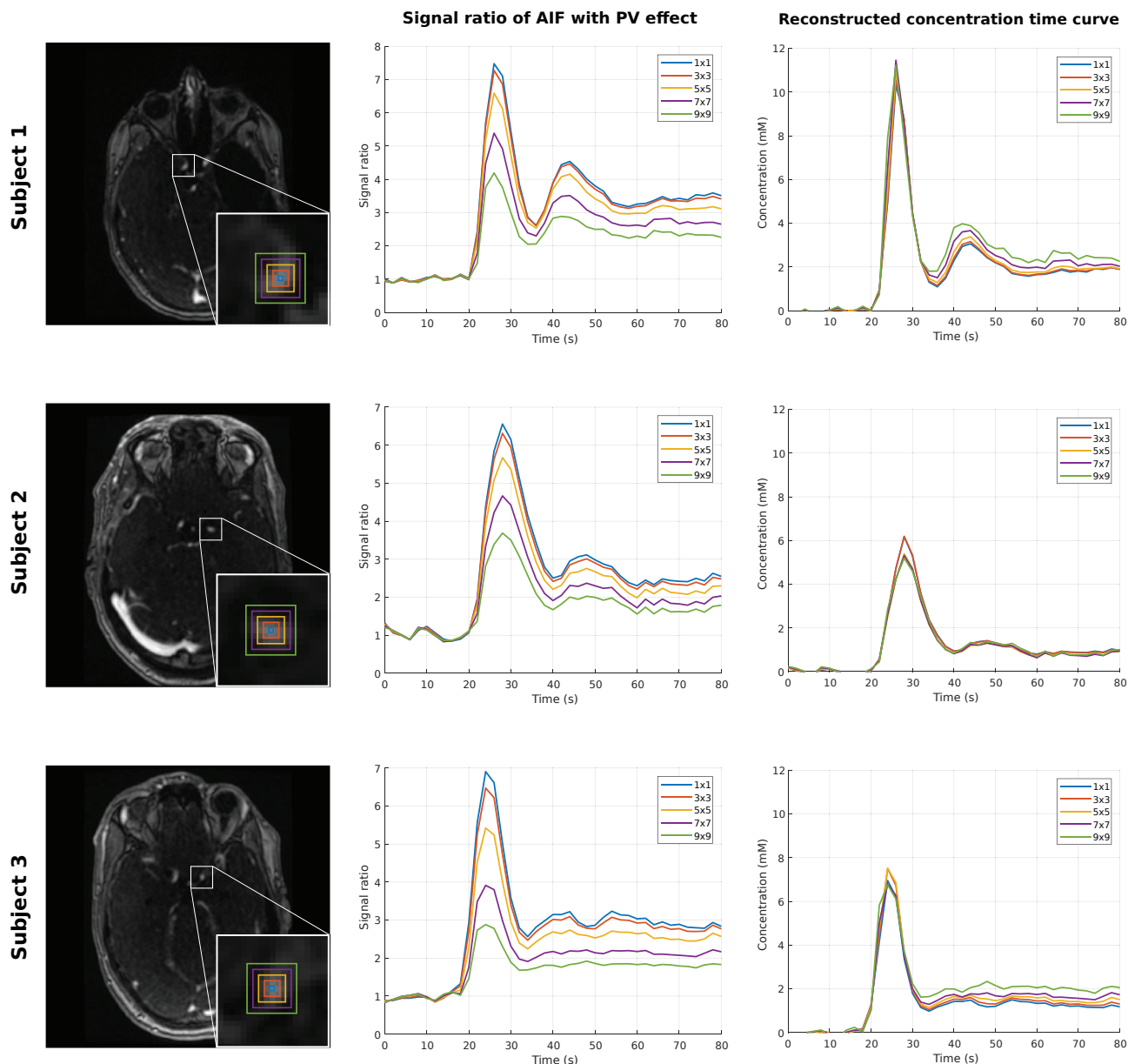


FIGURE 4 Simulation and compensation of increasing PVE in the internal carotid artery in three different subjects (top to bottom). The left column depicts a cross-section of the artery and the regions over which PVE is simulated (coloured squares). Mean signal-ratio curves within the kernel's footprint and reconstructed AIF concentration curves are shown in middle and right columns, respectively. Notice that only first 40 time points of the series are plotted for clarity reasons.

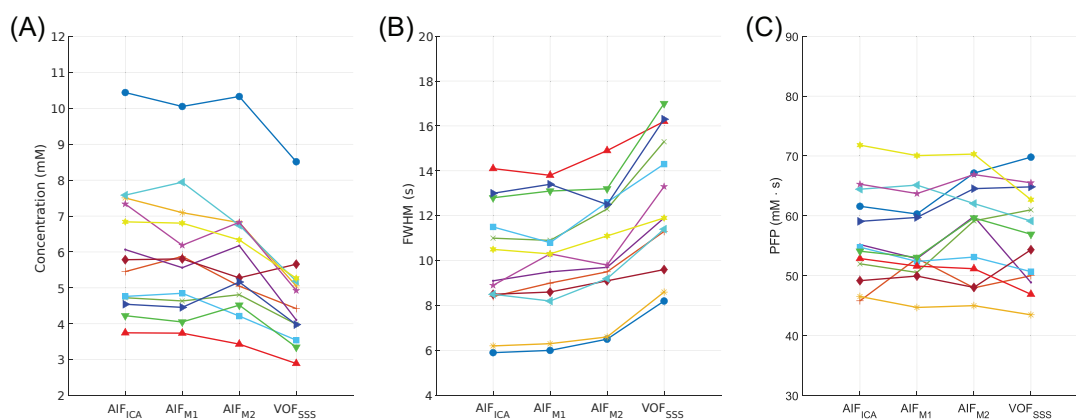
resolution may be sacrificed in order to accelerate the image acquisition, inherently resulting in mixing the arterial signal with tissue signals. A recent study emphasizes the importance of PVE correction for enhanced reproducibility of pharmacokinetic coefficients derived from DCE MRI.²⁰ To our knowledge, ours is the first study investigating the feasibility of correcting inflow effects and PVE simultaneously. To verify comprehensively the potential of the correction method, we performed realistic simulations, and also checked the method in an array of AIF measurements in clinical datasets. The method studied reconstructed the AIF accurately with marginal bias except for some unrealistic cases. This shows that the correction method has great potential for use in clinical DCE analysis.

When simulating only inflow effects, the method yielded a small bias (less than 3%) in the peak value and the width of the AIF (Figure 2b,c), irrespective of the extent of the inflow effect. The remaining bias results from T_2^* effects that were included in simulated signals. Indeed Figure S1 in the supplementary material shows the outcomes on simulated signals generated without any T_2^* effects, which do not exhibit a bias. At the same time, the interquartile range of the peak value and the AIF width increased for more severe inflow effects. This reflects that, with strong inflow (small n), a small error in the number of estimated pulses has a relatively large effect on the AIF parameters. Intuitively, this makes sense,

TABLE 1 Difference in estimated pulse number (n_d) and normalized root-mean-square error (NRMSE) of reconstructed AIFs with increasing PVE (i.e., applied kernel size) in comparison with data from the central arterial voxel.

	n_d (%)				NRMSE			
	3×3	5×5	7×7	9×9	3×3	5×5	7×7	9×9
Subject 1	−0.7	−5.3	−14.2	−26.6	0.008	0.016	0.032	0.055
Subject 2	−2.4	−8.8	−22.3	−33.0	0.003	0.008	0.039	0.046
Subject 3	−6.0	−16.2	−32.4	−44.1	0.023	0.038	0.074	0.098
Subject 3*	−2.3	−9.0	−26.0	−35.1	0.007	0.028	0.068	0.092
Subject 4*	−0.6	−1.4	−11.2	−22.4	0.004	0.019	0.036	0.080
Subject 5	−6.6	−12.0	−16.6	−26.7	0.023	0.036	0.054	0.145
Subject 6	−2.8	−6.7	−21.9	−30.7	0.003	0.021	0.016	0.023
Subject 6*	4.3	−3.2	−8.0	−17.9	0.035	0.011	0.025	0.023
Subject 7*	−3.1	−10.6	−21.2	−30.2	0.004	0.016	0.033	0.043
Subject 8	−4.9	−13.1	−24.9	−33.4	0.004	0.010	0.028	0.039
Subject 8*	−0.3	−6.5	−16.0	−24.5	0.006	0.012	0.025	0.034
Subject 9	−5.0	−11.7	−25.8	−36.4	0.004	0.015	0.022	0.033
Subject 10	−4.7	−13.3	−22.5	−32.0	0.007	0.022	0.029	0.040

*Patient received radiation therapy.

**FIGURE 5** (A) Peak values, (B) FWHMs, and (C) PFPs from AIF_{ICA}, AIF_{M1}, AIF_{M2} (applying inflow and partial voluming correction), and VOF_{SSS} (without any correction). Colours denote independent measurements. VOF_{SSS} had significantly lower peak value and higher FWHM than AIF_{ICA} and AIF_{M1}

since, closer to steady state (i.e., with small inflow), variation in the number of pulses affects the signal less, as such resulting in a more stable estimation of the AIF. At the same time, a small number of pulses suppresses the contrast of the signal-ratio curves, as can be observed in Figure 1b. This could also hinder the estimation of the number of pulses and affect the peak height and FWHM estimations.

When including PVE but applying the correct number of pulses (i.e., perfect correction of only the inflow effects), the peak value and AIF width became significantly affected by PVE, especially when approaching steady state (see Figure 3d,e). This shows the dilemma in clinical use of DCE imaging, in which an AIF is preferably derived from arteries as close as possible to the tissue of interest, which would minimize inflow effects, but at the same time includes arteries affected by PVE due to their small size. Taking both effects into account, the proposed method yielded only a small bias in both the peak value and FWHM of the reconstructed AIF concentration curves (cf. Figure 3b,c). This remaining (mild) bias might be due to unaccounted-for differences between partial volume and inflow effects. In particular, the stability of the estimation (i.e., the constantly small width and bias of the distributions), independent of PVE/degree of inflow, gives the technique high potential for clinical application.

Our experiments about mimicking PVE by averaging the signal over larger numbers of voxels surrounding a central arterial voxel confirm the robustness of the proposed approach, as larger PVE hardly affected the outcome. Robustness against such varying partial voluming is useful, as it can be difficult to delineate a region in an artery accurately in clinical DCE data. Simultaneously, however, it is important to ascertain that surrounding tissue exhibits the same enhancement timing as the studied artery. In particular, we observed that, as the averaging region in this

experiment started to overlap with a region exhibiting a later enhancement, the outcome became increasingly biased. The combination of such distinct enhancement profiles gave a distorted bolus peak profile, which resulted in erroneous correction. Thus, one should avoid applying our correction to AIF measurements in neighbourhoods with different vessels, as they may show varied enhancement timing, yielding a wrong outcome.

Measuring the AIF from the ICA is associated with less PVE compared with the MCA, but there are stronger inflow effects. Practically, the ICA may not always be covered by the image volume due to imaging limitations, for example, restrictions in scan time. In that case, the MCA could be an alternative, inherently at the expense of larger PVE. We studied both AIF sources to demonstrate the capability of our method with different combinations of inflow effect and PVE. We did not find a significant difference in peak value and FWHM between the measurements in the ICA and MCA (for both the M1 and M2 segments). However, a small decreasing trend in the AIF peak and an increasing trend in the FWHM from the M1 to M2 segment of the MCA seems visible in our data (Figure 5). Essentially, this corresponds with our simulation results, in which mild inflow effects combined with larger PVE caused increasing (albeit marginal) bias (Figure 3). Accordingly, we propose to apply the correction method practically to an AIF from the most upstream fragment of the covered vascular system, as that should give the most reliable outcome.

VOF measurement in the SSS has also been considered as a useful alternative to arterial measurement, due to limited inflow and PVE effects.³⁸ Indeed, by applying the correction algorithm to the measured signal-ratio curve from the SSS, a large number of excitation pulses was estimated (Figure S3). This signified that the spins were close to steady state. However, significantly lower peak values and increased FWHMs were found when comparing the VOF from the SSS with the AIF in the ICA or M1 segment of the MCA. This showed that the shape of the VOF was not in agreement with the AIF. We attribute this difference to increased dispersion of the contrast agent, limiting the usefulness of the SSS measurement as input of a DCE analysis. This corresponds with the results from Cramer et al,²⁰ who reported that the VOF measured in the SSS had a lower peak value than AIFs with PVE corrections; also, it was found that the VOF yielded low reproducibility, even though the VOF is theoretically less prone to inflow artefacts and PVE.

There are several limitations to our study. First, we did not have a real ground-truth AIF. Clearly, such a true AIF can only be measured from blood sampling, for which we did not have ethical approval. Furthermore, the method assumed a fixed area under the first bolus peak to estimate the underestimation of inflow and PVE. This might in reality vary across subjects and/or the vessel of interest. However, it was previously reported by Parker et al¹¹ that the relative standard error in this parameter is only 5.4%. In addition, we assumed that local extravasation of contrast agent can be neglected. The extravasation might affect the ROI signal in which the AIF is determined when the leakage is substantial or for large degrees of PVE. As such, the ROI for the AIF should not be selected near tumour tissue, but, for example, on the contralateral side of the brain. Finally, we did not study the effect of the AIF on the estimation of pharmacokinetic model parameters like K^{trans} in tumour regions, since we did not observe any clear leakage of contrast in the T_1 -weighted images in any of our patients (comparing the signal in the baseline DCE images with those after contrast injection).

6 | CONCLUSION

This study demonstrated the potential of a method to correct the AIF simultaneously for inflow effect and PVE. The method relies on interpreting larger PVE as increasing inflow effect. Although the SSS is less susceptible to the effects referred to, it was found not to be an appropriate source for the input function, as it showed increased dispersion of the GBCA. As a result, this would lead to overestimation of vascular permeability coefficients compared with the AIFs. Instead, applying the studied approach of deriving AIFs from arteries with proper correction of inflow and PVE could be a better strategy for DCE analysis.

ACKNOWLEDGEMENTS

We appreciate HollandPTC-Varian Consortium and Medical Delta Cancer Diagnostics 3.0 for supporting our project financially.

CONFLICT OF INTEREST

Author Marion Smits received a consultancy fee from Bracco and speaker fees from AuntMinnie and GE Healthcare (paid to institution). Author Matthias van Osch receives research support from Philips. No other conflict of interest was reported from other authors.

DATA AVAILABILITY STATEMENT

The code for the correction algorithm can be found at: https://github.com/Chih-Hsein/Inflow_PVE_correction. The image data that support the findings of this study are not publicly available, since their disclosure was not included in the informed consent.

ORCID

Chih-Hsien Tseng  <https://orcid.org/0000-0001-8692-6047>

Matthias J.P. van Osch  <https://orcid.org/0000-0001-7034-8959>

REFERENCES

1. Yankeelov T, Gore J. Dynamic Contrast Enhanced Magnetic Resonance Imaging in Oncology: Theory, Data Acquisition, Analysis, and Examples. *Current Med Imag Rev.* 2007;3(2):91-107.
2. Tuncbilek N, Karakas HM, Altaner S. Dynamic MRI in indirect estimation of microvessel density, histologic grade, and prognosis in colorectal adenocarcinomas. *Abdom Imag.* 2004;29(2):166-172.
3. Tuncbilek N, Karakas HM, Okten OO. Dynamic contrast-enhanced MRI in the differential diagnosis of soft tissue tumors. *Eur J Radiol.* 2005;53(3):500-505.
4. Medved M, Karczmar G, Yang C, Dignam J, Gajewski TF, Kindler H, Vokes E, MacEneaney P, Mitchell MT, Stadler WM. Semiquantitative analysis of dynamic contrast-enhanced MRI in cancer patients: Variability and changes in tumor tissue over time. *J Magn Res Imag.* 2004;20(1):122-128.
5. Arasu VA, Chen RC-Y, Newitt DN, Chang CB, Tso H, Hylton NM, Joe BN. Can Signal Enhancement Ratio (SER) Reduce the Number of Recommended Biopsies without Affecting Cancer Yield in Occult MRI-detected Lesions? *Acad Radiol.* 2011;18(6):716-721.
6. Lavini C, de Jonge MC, van de Sande MGH, Tak PP, Nederveen AJ, Maas M. Pixel-by-pixel analysis of DCE MRI curve patterns and an illustration of its application to the imaging of the musculoskeletal system. *Magn Res Imag.* 2007;25(5):604-612.
7. Khalifa F, Soliman A, El-Baz A, Abou El-Ghar M, El-Diasty T, Gimelfarb G, Ouseph R, Dwyer AC. Models and methods for analyzing DCE-MRI: A review. *Med Phys.* 2014;41(12):124301.
8. Tofts PS, Brix G, Buckley DL, Evelhoch JL, Henderson E, Knopp MV, Larsson HBW, Lee T-Y, Mayr NA, Parker GJM, Port RE, Taylor J, Weisskoff RM. Estimating kinetic parameters from dynamic contrast-enhanced t1-weighted MRI of a diffusible tracer: Standardized quantities and symbols. *J Magn Res Imag.* 1999;10(3):223-232.
9. Essig M, Shiroishi MS, Nguyen TB, Saake M, Provenzale JM, Enterline D, Anzalone N, Dörfler A, Rovira, Wintermark M, Law M. Perfusion MRI: The Five Most Frequently Asked Technical Questions. *Am J Roentgenol.* 2013;200(1):24-34.
10. Okuchi S, Roja Garcia A, Ulyte A, Lopez I, Ušinskienė J, Lewis M, Hassanein SM, Sanverdi E, Golay X, Thust S, Panovska Griffiths J, Bisdas S. Diagnostic accuracy of dynamic contrast enhanced perfusion MRI in stratifying gliomas: A systematic review and meta analysis. *Cancer Med.* 2019;8(12):5564-5573.
11. Parker GJM, Roberts C, Macdonald A, Buonaccorsi GA, Cheung S, Buckley DL, Jackson A, Watson Y, Davies K, Jayson GC. Experimentally-derived functional form for a population-averaged high-temporal-resolution arterial input function for dynamic contrast-enhanced MRI. *Magn Res Med.* 2006;56(5):993-1000.
12. Rijpkema M, Kaanders JHAM, Joosten FBM, van der Kogel AJ, Heerschap A. Method for quantitative mapping of dynamic MRI contrast agent uptake in human tumors. *J Magn Res Imag.* 2001;14(4):457-463.
13. Ashton E, Raunig D, Ng C, Kelcz F, McShane T, Evelhoch J. Scan-rescan variability in perfusion assessment of tumors in MRI using both model and data-derived arterial input functions. *J Magn Res Imag.* 2008;28(3):791-796.
14. Calamante F. Bolus dispersion issues related to the quantification of perfusion MRI data. *J Magn Res Imag.* 2005;22(6):718-722.
15. van Osch MJP, Vonken E-PA, Bakker CJG, Viergever MA. Correcting partial volume artifacts of the arterial input function in quantitative cerebral perfusion MRI. *Magn Res Med.* 2001;45(3):477-485.
16. Hansen AE, Pedersen H, Rostrup E, Larsson HBW. Partial volume effect (PVE) on the arterial input function (AIF) in T1-weighted perfusion imaging and limitations of the multiplicative rescaling approach. *Magn Res Med.* 2009;62(4):1055-1059.
17. Harrer JU, Parker GJM, Haroon HA, Buckley DL, Embelton K, Roberts C, Balériaux D, Jackson A. Comparative study of methods for determining vascular permeability and blood volume in human gliomas. *J Magn Res Imag.* 2004;20(5):748-757.
18. Keil VC, Mädler B, Gieseke J, Fimmers R, Hattingen E, Schild HH, Hadizadeh DR. Effects of arterial input function selection on kinetic parameters in brain dynamic contrast-enhanced MRI. *Magn Res Imag.* 2017;40:83-90.
19. Thrippleton MJ, Backes WH, Sourbron S, Ingrisch M, van Osch MJP, Dichgans M, Fazekas F, Ropele S, Frayne R, van Oostenbrugge RJ, Smith EE, Wardlaw JM. Quantifying blood brain barrier leakage in small vessel disease: Review and consensus recommendations. *Alzheimer's Dementia.* 2019;15(6):840-858.
20. Cramer SP, Larsson HBW, Knudsen MH, Simonsen HJ, Vestergaard MB, Lindberg U. Reproducibility and Optimal Arterial Input Function Selection in Dynamic Contrast enhanced Perfusion MRI in the Healthy Brain. *J Magn Res Imag.* 2022;57:1229-1240.
21. Roberts C, Little R, Watson Y, Zhao S, Buckley DL, Parker GJM. The effect of blood inflow and B1-field inhomogeneity on measurement of the arterial input function in axial 3D spoiled gradient echo dynamic contrast-enhanced MRI. *Magn Res Med.* 2011;65(1):108-119.
22. Ivancevic MK, Zimine I, Montet X, Hyacinthe J-N, Lazeyras F, Foxall D, Vallée J-P. Inflow effect correction in fast gradient-echo perfusion imaging. *Magn Res Med.* 2003;50(5):885-891.
23. Garpebring A, Wirestam R, Ostlund N, Karlsson M. Effects of inflow and radiofrequency spoiling on the arterial input function in dynamic contrast-enhanced MRI: a combined phantom and simulation study. *Magn Res Med.* 2011;65(6):1670-1679.
24. Garpebring A, Wirestam R, Yu J, Askund T, Karlsson M. Phase-based arterial input functions in humans applied to dynamic contrast-enhanced MRI: potential usefulness and limitations. *Magn Res Mater Phys, Biol Med.* 2011;24(4):233-245.
25. Materne R, Smith AM, Peeters F, Dehoux JP, Keyeux A, Horsmans Y, Van Beers BE. Assessment of hepatic perfusion parameters with dynamic MRI. *Magn Res Med.* 2002;47(1):135-142.
26. Ning J, Schubert T, Johnson KM, Roldán-Alzate A, Chen H, Yuan C, Reeder SB. Vascular input function correction of inflow enhancement for improved pharmacokinetic modeling of liver DCE-MRI. *Magn Res Med.* 2018;79(6):3093-3102.
27. van Schie JN, Lavini C, van Vliet LJ, Vos FM. Estimating the arterial input function from dynamic contrast-enhanced MRI data with compensation for flow enhancement (I): Theory, method, and phantom experiments. *J Magn Res Imag: JMRI.* 2018;47(5):1190-1196.
28. Orton MR, D'Arcy JA, Walker-Samuel S, Hawkes DJ, Atkinson D, Collins DJ, Leach MO. Computationally efficient vascular input function models for quantitative kinetic modelling using DCE-MRI. *Phys Med Biol.* 2008;53(5):1225-1239.
29. de Simone G, Devereux RB, Daniels SR, Mureddu G, Roman MJ, Kimball TR, Greco R, Witt S, Contaldo F. Stroke Volume and Cardiac Output in Normotensive Children and Adults. *Circulation.* 1997;95(7):1837-1843.
30. Zhang X, Petersen ET, Ghariq E, De Vis JB, Webb AG, Teeuwisse WM, Hendrikse J, van Osch MJP. In vivo blood T1 measurements at 1.5 T, 3 T, and 7 T. *Magn Res Med.* 2013;70(4):1082-1086.

31. Petrovic A, Krauskopf A, Hassler E, Stollberger R, Scheurer E. Time related changes of T1, T2, and T2* of human blood in vitro. *Forensic Sci Int.* 2016; 262:11-17.
32. Shen Y, Goerner FL, Snyder C, Morelli JN, Hao D, Hu D, Li X, Runge VM. T1 relaxivities of gadolinium-based magnetic resonance contrast agents in human whole blood at 1.5, 3, and 7 T. *Investig Radiol.* 2015;50(5):330-338.
33. Calamante F, Vonken E-PA, van Osch MJP. Contrast agent concentration measurements affecting quantification of bolus-tracking perfusion MRI. *Magn Res Med.* 2007;58(3):544-553.
34. Pedersen M, Klarhöfer M, Christensen S, Ouallet J-C, Østergaard L, Dousset V, Moonen C. Quantitative cerebral perfusion using the PRESTO acquisition scheme. *J Magn Res Imag.* 2004;20(6):930-940.
35. Fritsch FN, Carlson RE. Monotone Piecewise Cubic Interpolation. *SIAM J Numer Anal.* 1980;17(2):238-246.
36. Saranathan M, Rettmann DW, Hargreaves BA, Clarke SE, Vasanawala SS. Differential subsampling with cartesian ordering (DISCO): A high spatio-temporal resolution dixon imaging sequence for multiphasic contrast enhanced abdominal imaging. *J Magn Res Imag.* 2012;35(6):1484-1492.
37. Lim WH, Park JS, Park J, Choi SH. Assessing the reproducibility of high temporal and spatial resolution dynamic contrast-enhanced magnetic resonance imaging in patients with gliomas. *Sci Rep.* 2021;11(1):23217.
38. Ewing JR, Knight RA, Nagaraja TN, Yee JS, Nagesh V, Whitton PA, Li L, Fenstermacher JD. Patlak plots of Gd DTPA MRI data yield blood brain transfer constants concordant with those of ¹⁴C sucrose in areas of blood brain opening. *Magn Res Med.* 2003;50(2):283-292.

SUPPORTING INFORMATION

Additional supporting information can be found online in the Supporting Information section at the end of this article.

How to cite this article: Tseng C-H, Nagtegaal MA, van Osch MJP, et al. Arterial input function estimation compensating for inflow and partial voluming in dynamic contrast-enhanced MRI. *NMR in Biomedicine.* 2024;e5225. doi:10.1002/nbm.5225

APPENDIX A

In this Appendix, we aim to show mathematically that the PVE has a similar effect to the inflow effect on DCE-AIF measurement.

Our derivation starts with writing out the expression for the spoiled gradient echo signal as a function of the excitation pulse number n , by combining Equations (1)–(3):

$$S(n) = \sin\alpha \cdot M_0 \cdot \left[\left(1 - \frac{1 - e^{-T_R/T_1}}{1 - \cos\alpha \cdot e^{-T_R/T_1}} \right) \cdot \left(\cos\alpha \cdot e^{-T_R/T_1} \right)^n + \frac{1 - e^{-T_R/T_1}}{1 - \cos\alpha \cdot e^{-T_R/T_1}} \right] \cdot e^{-T_E/T_2^*}. \quad (\text{A1})$$

Observe that in this expression the term $M_0 \cdot (1 - e^{-T_R/T_1}) / (1 - \cos\alpha \cdot e^{-T_R/T_1})$ is equal to the steady-state magnetization given in Equation (4). Furthermore, the T_1 and T_2^* parameters are modulated by the contrast agent concentration as defined in Equations (5) and (6), respectively. Taking these aspects into account, Equation (A1) can be rewritten as

$$S(C, n) = \sin\alpha \cdot \left[(M_0 - M_z(C, \infty)) \cdot \left(\cos\alpha \cdot e^{-T_R/T_1(C)} \right)^n + M_z(C, \infty) \right] \cdot e^{-T_E/T_2^*(C)}. \quad (\text{A2})$$

In the steady state, that is, with very large n , this expression simplifies to $S(C, \infty) = \sin\alpha \cdot M_z(C, \infty) \cdot e^{-T_E/T_2^*(C)}$. Based on this, by reshuffling the terms the former equation yields

$$S(C, n) = M_0 \cdot \sin\alpha \cdot \left(\cos\alpha \cdot e^{-T_R/T_1(C)} \right)^n \cdot e^{-T_E/T_2^*(C)} + \left[1 - \left(\cos\alpha \cdot e^{-T_R/T_1(C)} \right)^n \right] \cdot S(C, \infty). \quad (\text{A3})$$

In the T_1 -weighted DCE sequence, the echo time is usually small (≈ 1 ms), so that $e^{-T_E/T_2^*(C)} \approx 1$. Additionally, $(\cos\alpha \cdot e^{-T_R/T_1(C)})^n$ can be conceived as a weighting factor $w(C, n)$ that ranges from 0 (for large n) to 1 (for small n). As a result, the above equation can be approximated by

$$S(C, n) \approx w(C, n) \cdot M_0 \cdot \sin\alpha + [1 - w(C, n)] \cdot S(C, \infty). \quad (\text{A4})$$

In this last equation, $M_0 \cdot \sin\alpha$ is a constant term. Thus, the AIF signal ($S(C, n)$) indeed approximates the steady-state AIF with large n , while a constant signal is increasingly mixed in with decreasing n . This equation is compatible with Equation (14). As such, flow can be considered as a PVE in which a fraction $w(C, n)$ of the background signal $M_0 \cdot \sin\alpha$ is combined with the foreground AIF.